The Aeronautical Journal, Volume 125, Issue 1291:
The 25th ISABE Conference special issue, September 2021, pp. 1519-1541
DOI:10.1017/aer.2021.10

Numerical investigation of the breakup mode and trajectory of liquid jet in a gaseous crossflow at elevated conditions

Yu Zhu[1,2], Xiaoxiao Sun[2], Vishal Sethi[2], Pierre Gauthier[2], Shu Guo[1], Ruiqiang Bai[1] and Dongbo Yan[1]

Zhuyu0324@qq.com

1. AECC Shenyang Engine Research Institute, Department of Combustion, Shenyang, China
2. Cranfield University, School of Aerospace, Transport and Manufacturing, Cranfield, UK

ABSTRACT

The commercial CFD software STAR-CCM+ was used to simulate the flow and breakup characteristics of a liquid jet injected into the gaseous crossflow (LJIC) under real engine operating conditions. The reasonable calculation domain geometry and flow boundary conditions were obtained based on a civil aviation engine performance model similar to the Leap-1B engine which was developed using the GasTurb software and the preliminary design results of its low-emission combustor. The Volume of Fluid (VOF) model was applied to simulate the breakup feature of the near field of LJIC. The numerical method was validated and calibrated through comparison with the public test data at atmospheric conditions. The results showed that the numerical method can capture most of the jet breakup structure and predict the jet trajectory with the error not exceeding ±5%. The verified numerical method was applied to simulate the breakup of LJIC at the real engine operating condition. The breakup mode of LJIC was shown to be surface shear breakup at elevated condition. The trajectory of the liquid jet showed good agreement with Ragucci's empirical correlation.

Keywords: Jet trajectory; Simulation; VOF; Breakup; Elevated condition

NOMENCLATURE

CFD	Computational Fluid Dynamics
HRIC	High-Resolution Interface Capturing
LJIC	Liquid Jet in Crossflow
K-H	Kelvin–Helmholtz
SST	Shear-Stress Transport
TAPS	Twin Annular Premixing Swirler
VOF	Volume of Fluid

Symbols

c_p	specific heat capacity, J/kg/K
c_s	volume concentration of component s
C	constant
d	diameter, m
div	vector symbol
D	diffusion coefficient
E	energy, J
F	force, N
k	heat transfer coefficient, W/m/K
Oh	Ohnesorge number
P	pressure, Pa
q	jet-to-crossflow momentum flux ratio
Re	Reynolds number
S	source term
t	time, s
T	temperature, K
$\boldsymbol{u}$	velocity vector, m/s
v	velocity, m/s
W	mass flow rate, kg/s
We	Weber number
x	axial distance, m
y	radial distance, m
α_q	the q-phase fluid volume fraction in the unit
μ	dynamic viscosity, kg/m/s
μ_t	turbulent viscosity
σ	surface tension, N/m
ρ	density, kg/m^3
τ	viscous stress, Pa
ω	specific dissipation rate

Subscript

ch	channel
g	gas
j	jet
w	water

1.0 INTRODUCTION

Liquid Jet in gaseous Crossflow (LJIC) technology provides good fuel atomization characteristics and enables fuel and air mixing uniformly in a short distance, which shows a good application prospect in low emissions combustion systems. Although LJIC technology has various applications, the main concern here is its application in the combustor of an aero-engine. One famous case is the Twin Annular Premixing Swirler (TAPS) technology that was developed by General Electric company, which employs LJIC in the main stage fuel injection, shows a 50% margin of NOx emission relative to the CAEP 6 standard[1].

Whether the liquid jet is non-turbulent or turbulent will affect the shape of the primary breakup. Wu et al.[2] proposed the criteria for the occurrence of non-turbulent and turbulent liquid jets. At high Re_j, when the length/diameter ratio of the nozzle is less than 4-6, the surface of the liquid jet is smooth without reattachment which meant a non-turbulent flow. In contrast, when the length/diameter ratio is relatively high, a fully developed turbulence flow with high Re_j will appear at the nozzle exit. Most nozzles in aero-engines produce non-turbulent jets. Therefore, non-turbulent jets are mainly discussed in this paper.

Many empirical diagrams have been proposed in the literature for predicting the primary breakup regimes of non-turbulent liquid jets injected into subsonic gaseous crossflows. The most commonly used of these diagrams was the $We_g - q$ diagram, which was first proposed by Wu et al.[3]. It classified the breakup features of liquid jets observed in the crossflow and was shown in Figure 1. Wu et al. believed that, since the breakup of liquid jets and droplets in crossflow was caused by aerodynamics, the knowledge of the secondary breakup of droplets caused by the aerodynamic may apply to the primary breakup of liquid jets. Through q and We_g, they divided the breakup characteristics of the liquid jet observed in cross-flow into two main regimes (i.e., column breakup and surface breakup). They concluded that column breakup occurred at low q and/or low We_g, and surface breakup can be observed at high q and/or high We_g. The column breakup area is also divided into four sub-areas in the map based on We_g. For $We_g < 11$, the breakup phenomenon showed as the enhanced capillary breakup. At increased Weber numbers ($11 < We_g < 30$), transitions occur, both column breakup and bag breakup exist. In the case of $30 < We_g < 90$, the breakup process is multi-mode, and the final shear breakup process occurs when $We_g > 90$. The breakup regime map shows different jet breakup regimes, and visual observations based on the work of Wu et al. indicated the transition boundary between the column and the surface breakup. However, the transition is a gradual process, there is no clear threshold to distinguish the two systems, and further research needs to be done to determine the mechanism of this transition.

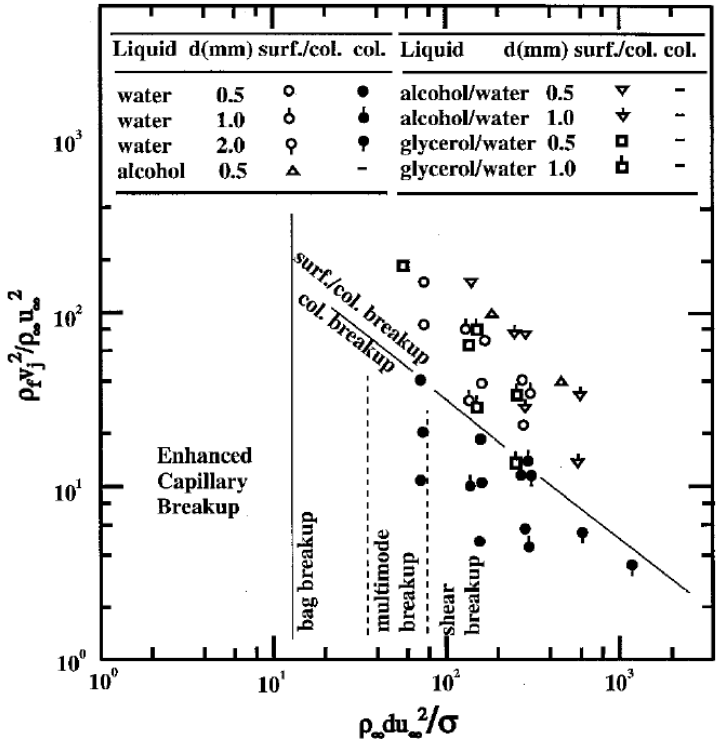

Figure 1 Regime diagram of the breakup of LJIC[3]

The trajectory of the liquid jet is an important characteristic of LJIC because they directly affect the distribution of the fuel spray in the combustion zone, and therefore the evaporation of the fuel and its mixing rate with the air. In order to describe the trajectory of LJIC, researchers have proposed many empirical and phenomenological correlations based on non-dimensional parameters (such as q, Re_j, Re_g, We_g, We_j, viscosity ratio and density ratio). However, because of the complex physics of the two-phase flow field of LJIC, the trajectory of the liquid jet depends on many variables, such as the liquid properties, airflow conditions, shape of the nozzle and measurement instruments, which resulted in considerable dispersion of these correlations. These dispersions are difficult to eliminate completely but can be minimized by classifying these correlations into different categories based on test conditions. Although most published studies have been performed under atmospheric conditions, some studies have been performed at elevated crossflow temperature and pressure. The trajectory of LJIC will change with the test conditions since the changes in the test conditions will cause changes in liquid and gas properties. Table 1 shows a few published correlations about the LJIC trajectory at elevated conditions.

Table 1
Correlations of the trajectory of LJIC at elevated conditions

No.	Correlations	q	We_g	x/d_j	T(K)	P(bar)	Reference
1	$y/d_j = 15q^{0.5}(x/d_j)^{0.33}We_g^{-0.41}(\mu_j/\mu_w)^{-0.027}$	2.2–75	700–1580	0–12	350–475	3.8–6.5	Masuda and McDonell[4]
2	$y/d_j = 0.909q^{0.476}(x/d_j)^{0.35}We_g^{-0.128}Re_g^{0.135}$	12.2–71.4	10.4-410.5	0–12	300, 600	10, 20	Bellofiore et al. [5]
3	$y/d_j = 2.28q^{0.422}(x/d_j)^{0.367}We_g^{-0.015}(\mu_g/\mu_{air,300K})^{0.186}$	5–280	7-340	0–12	600	20	Ragucci et al. [6]

4	$y/d_j = 1.44\ln(1.06(x/d_j) + 1)q^{0.4356}We_g^{0.01147}(T/T_0)^{0.295}$	16–76	399–1630	0–40	280–650	5–20	Li et al. [7]
5	$y/d_j = 0.191q^{0.3}(x/d_j)^{0.43}Re_{ch}^{0.12}Re_j^{0.14}$	10–80	20–487	0–17	298–573	2.1–5.2	Eslamian et al. [8]
6	$y/d_j = 13.31q^{0.40}\left(\frac{x}{d_j} + 0.5\right)^{0.27}We_g^{0.14}Oh_g^{-0.20}Oh_j^{0.65}$	8-181	7-298	0–25	298–573	2.1–5.2	Amighi et al. [9]

Although the correlations in Table 1 cover a wide range of q, We_g, crossflow temperature and pressure, there are still some operating conditions of aero-engine combustors beyond this scope. At the cruise condition of a typical civil turbofan engine, the LJIC in the combustor may have much lower q which less than 2, much higher We_g which over 2000, and also higher crossflow temperature. Whether these existing correlations can be used in extended range need further investigation.

Due to safety considerations and the limitation of the ability of test facilities, in experimental researches, it is difficult to meet the high-temperature and high-pressure conditions in the real operating conditions of the engine. But with the development of high-performance computing technology, CFD has begun to enter the arena of LJIC research[10-17]. The effects of various parameters like liquid viscosity, liquid/gas density ratio, momentum flux ratio, and crossflow Weber number on liquid jets were investigated using numerical methods. The VOF method was the mostly used technique to capture the precise free boundary surface. Results showed that the predicted liquid jet trajectory matched well with published experimental data sets. The numerical simulation has showed its potential to be a useful tool in studying LJIC.

This article aims to assess the ability of the commercial CFD software STAR-CCM+ to simulate LJIC and study the flow and breakup characteristics of the LJIC under real engine operating conditions and predict the jet trajectory of LJIC simultaneously. Due to the lack of available test data at high-temperature and high-pressure conditions, the numerical method was validated and calibrated through comparing with the public test data at atmospheric conditions. Then the verified numerical method was applied to simulate the breakup of LJIC at the real engine operating condition. A database of numerical models was created to be further evaluated, validated and calibrated from a planned experimental campaign. Finally, the existing correlations will be compared with the numerical results to assess their applicability at real engine operating conditions.

2.0 NUMERICAL METHODS

Numerical simulations were performed on STAR-CCM+ (Version 14.04.013/R8) through the high performance computation center of Cranfield University.

2.1 Control Equations

Control Equations include mass conservation equation, momentum conservation equation, energy conservation equation and component mass conservation equation are listed in (1)-(6).

$$\frac{\partial \rho}{\partial t} + \frac{\partial(\rho u)}{\partial x} + \frac{\partial(\rho v)}{\partial y} + \frac{\partial(\rho w)}{\partial z} = 0 \qquad \dots (\ 1\ )$$

$$\frac{\partial(\rho u)}{\partial t} + \mathrm{div}(\rho u \boldsymbol{u}) = -\frac{\partial p}{\partial x} + \frac{\partial \tau_{xx}}{\partial x} + \frac{\partial \tau_{yx}}{\partial y} + \frac{\partial \tau_{zx}}{\partial z} + F_x \qquad \dots (\ 2\ )$$

$$\frac{\partial(\rho v)}{\partial t} + \mathrm{div}(\rho v \boldsymbol{u}) = -\frac{\partial p}{\partial y} + \frac{\partial \tau_{xy}}{\partial x} + \frac{\partial \tau_{yy}}{\partial y} + \frac{\partial \tau_{zy}}{\partial z} + F_y \qquad \dots (\ 3\ )$$

$$\frac{\partial(\rho w)}{\partial t} + \mathrm{div}(\rho w \boldsymbol{u}) = -\frac{\partial p}{\partial z} + \frac{\partial \tau_{xz}}{\partial x} + \frac{\partial \tau_{yz}}{\partial y} + \frac{\partial \tau_{zz}}{\partial z} + F_z \qquad \ldots (\ 4\ )$$

$$\frac{\partial(\rho T)}{\partial t} + \mathrm{div}(\rho \boldsymbol{u} T) = \mathrm{div}\left(\frac{k}{c_p}\mathrm{grad}\, T\right) + S_T \qquad \ldots (\ 5\ )$$

$$\frac{\partial(\rho c_s)}{\partial t} + \mathrm{div}(\rho \boldsymbol{u} c_s) = \mathrm{div}\big(D_s\ \mathrm{grad}\ (\rho c_s)\big) + S_s \qquad \ldots (\ 6\ )$$

2.2 Turbulence Model

The SST (shear-stress transport) $k-\omega$ model has seen fairly wide application in the aerospace industry. The transport equations for the kinetic energy k and specific dissipation rate ω are :

$$\frac{\partial(\rho k)}{\partial t} + \nabla\cdot(\rho k\bar{\boldsymbol{u}}) = \nabla\cdot[(\mu + \sigma_k\mu_t)\nabla k] + P_k - \rho\beta^* f_{\beta^*}(\omega k - \omega_0 k_0) + S_k \qquad \ldots (\ 7\ )$$

$$\frac{\partial(\rho\omega)}{\partial t} + \nabla\cdot(\rho\omega\bar{\boldsymbol{u}}) = \nabla\cdot[(\mu + \sigma_\omega\mu_t)\nabla\omega] + P_\omega - \rho\beta f_\beta(\omega^2 - \omega_0^2) + S_\omega \qquad \ldots (\ 8\ )$$

where $\bar{u}$ is the mean velocity, μ is the dynamic viscosity, σ_k and σ_ω are model coefficients, P_k and P_ω are production terms, f_{β^*} is the free-shear modification factor, f_β is the vortex-stretching modification factor, S_k and S_ω are the user-specified source terms, k_0 and ω_0 are the ambient turbulence values that counteract turbulence decay.

2.3 Near-Wall Treatment

The near-wall area can be roughly divided into three layers. The innermost layer adjacent to the wall is the viscous sublayer; the outer layer is the log-law layer; between them, is the buffer layer. In STAR-CCM+ the continuous functions which are called blended wall functions (all y+ wall treatment) are used to cover all three sublayers. They represent the buffer layer by appropriately blending the viscous sublayer and the log layer.

2.4 VOF Model

The principle of the VOF model is the tracking technique for two or more immiscible fluid interfaces on a fixed Eulerian grid. In the calculation equation of the VOF model, each phase fluid shares a system of equations, and the volume fraction of each phase is tracked throughout the computational domain. In each control volume, the sum of the volume fractions of all phases is one. As long as the volume fraction of each phase at each point in the calculation domain is known, the fields of all variables and physical properties are shared by the phases and represent the volume average. Thus, depending on the value of the volume fraction, the variables and physical properties within any unit are either representatives of one phase or representative of a multiphase mixture. By solving the continuity equation for one or more phase volume fractions, the interface between the phases can be tracked. The continuity equation for the q-phase volume fraction is:

$$\frac{1}{\rho_q}\left[\frac{\partial}{\partial t}\left(\alpha_q\rho_q\right) + \nabla\cdot\left(\alpha_q\rho_q\overrightarrow{v_q}\right) = S_{\alpha_q} + \sum_{p=1}^{n}\left(\dot{m}_{pq} - \dot{m}_{qp}\right)\right] \qquad \ldots (\ 9\ )$$

where α_q is the fluid volume fraction of the q-phase, ρ_q is the physical density of the q-phase, $\overrightarrow{v_q}$ is the velocity of the q-phase, $\dot{m}_{qp}$ is the mass transfer from phase q to phase p, $\dot{m}_{pq}$ is the mass transfer from phase p to phase q, S_{α_q} is the source term with a default value of zero and can also be specified as a constant or user-defined quality source term.

Phase interface tracking is the focus of two-phase flow simulation. An important quality of a system of immiscible phases (for example, air and water) is that the fluids always remain separated by a sharp interface. The High-Resolution Interface Capturing (HRIC)

scheme is designed to mimic the convective transport of immiscible fluid components, resulting in a scheme that is suited for tracking sharp interfaces.

2.5 Gridding Strategy and Refinement

A trimmed grid was generated in the computational domain using the built-in meshing module of STAR-CCM+ software. Since the very fine mesh was required in the VOF model to accurately capture the free boundary surfaces of fluids between different phases, the mesh in the areas where the free boundary surfaces of fluids between different phases exist in the calculation domain was refined. The refinement process of the grid was artificially processed during the calculation process. Both the validation case and the simulation of LJIC at real engine operating condition employed the same gridding strategy and refinement method.

2.6 Model Selection

The calculation used an implicit unsteady solver, and the time-step was set to be 0.1 μs (1E-7 s). The turbulence model adopted the SST k-ω double equation eddy viscosity model, and the near-wall area adopted all y+ wall treatment. The multiphase model adopted the VOF model to capture the accurate free boundary surface.

3.0 VALIDATION OF NUMERICAL METHOD

Before performing the simulation of LJIC at real engine conditions, the numerical method must be validated through experimental data. Because of the absence of the experimental data under high-temperature and high-pressure, the validating simulation was performed at atmospheric conditions. Parameters for comparison between simulation and experimental data included jet trajectory, the morphology and mechanism of the primary breakup. The experiment performed by Stenzler et al.[18] was chosen to validate the numerical simulation method.

3.1 Calculation Domain

In the experiment, the crossflow pipe had a rectangle cross-section with the geometry of 25.8×28.9 ×100 mm (Height × Width× Length). In the calculation, in order to save calculation time, the setting of the calculation domain was smaller than the real experimental pipeline, which was 25.8×2.54 ×25.4 mm (Height × Width× Length) and was shown in Figure 2. The axial location of the nozzle was 5.08 mm after the crossflow inlet, and the liquid used in the experiment was acetone.

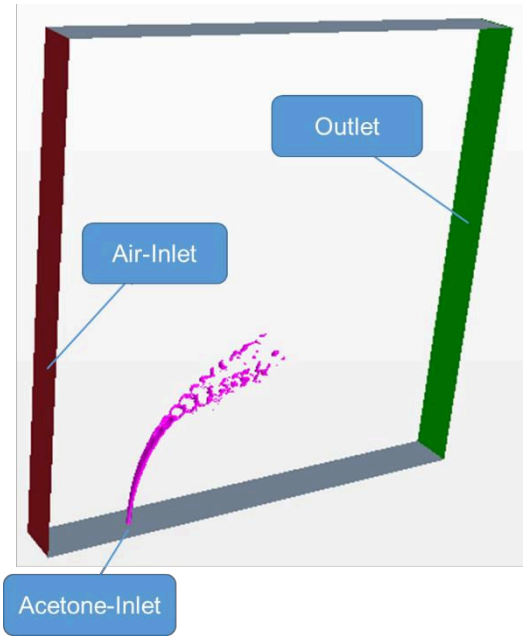

Figure 2 Schematic of the calculation domain

3.2 Calculation Grid

The refined mesh is shown in Figure 3. After the final refinement, the finest grid size was 0.00635mm, and the size of the grid was 22.1 million approximately.

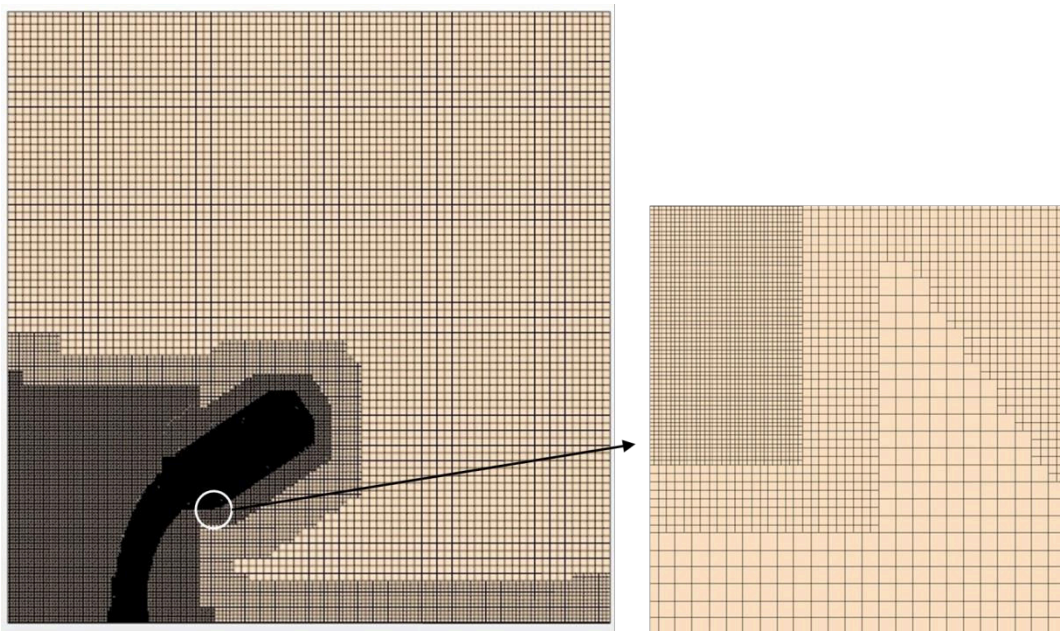

Figure 3 Mesh at centre plane and zoomed view of mesh refinement

3.3 Boundary Conditions

Since the computing domain used a smaller width to save computing resources, the wall boundaries on both sides of the computing domain were set to periodic boundaries. The liquid was set to acetone in the simulation to be consistent with the test. The detailed boundary conditions for crossflow and liquid jet are shown in Table 2.

Table 2
Boundary conditions of crossflow and liquid jet

Jet diameter (d_j)	0.254 mm
Jet velocity (v_j)	7.10 m/s
Crossflow velocity (v_g)	30.0 m/s
Jet density (ρ_j)	790 kg/m^3
Crossflow density (ρ_g)	1.217 kg/m^3
Jet viscosity (μ_j)	3.06E-4 kg/m/s
Crossflow viscosity (μ_g)	1.86E-5 kg/m/s
Surface tension (σ)	0.0235 N/m
Crossflow pressure (P)	101 kPa
Jet temperature (T)	291 K
Crossflow temperature (T)	291 K
Momentum ratio (q)	36
Jet Weber number (We_j)	430.4
Crossflow Weber number (We_g)	11.8
Jet Reynolds number (Re_j)	4655.8

Crossflow Reynolds number (Re_g)	499.8
Jet Ohnesorge number (Oh_j)	0.0045

Since the crossflow velocity distribution in the wind tunnel had been measured in the reference, here the crossflow velocity distribution in the height direction at the air inlet boundary used the fitted experimental data, as shown in Figure 4. Considering that the width of the calculation domain was small, the crossflow velocity distribution in the width direction was assumed to be uniform. At the same time, as the complete geometry of the nozzle was given, the nozzle was modelled and simulated before the simulation of LJIC, and the detailed velocity distribution at the nozzle exit was obtained and set as the liquid inlet boundary condition. The contour map of the velocity distribution at the nozzle exit is shown in Figure 5. As can be seen from the figure, the velocity in the central area of the liquid jet was about 8.5 m/s, which was higher than the average velocity of 7.1 m/s that was calculated based on the volume flux and the nozzle area. Conversely, the liquid velocity near the nozzle wall area was lower than the average velocity.

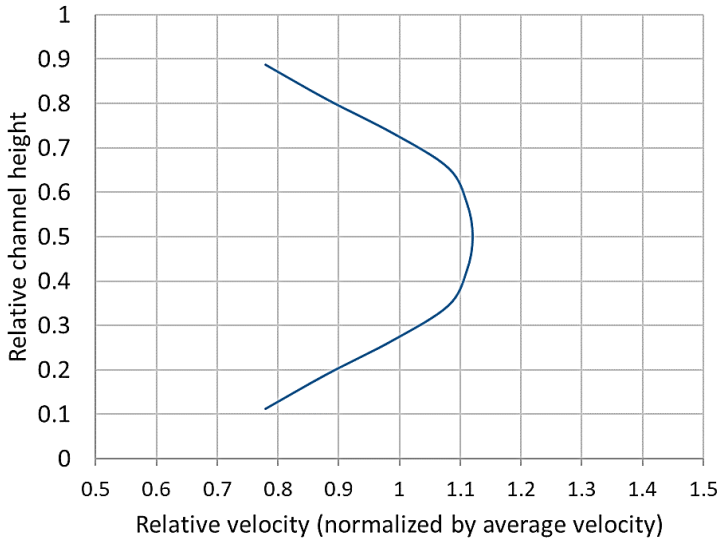

Figure 4 Fitted velocity profile at the injection plane

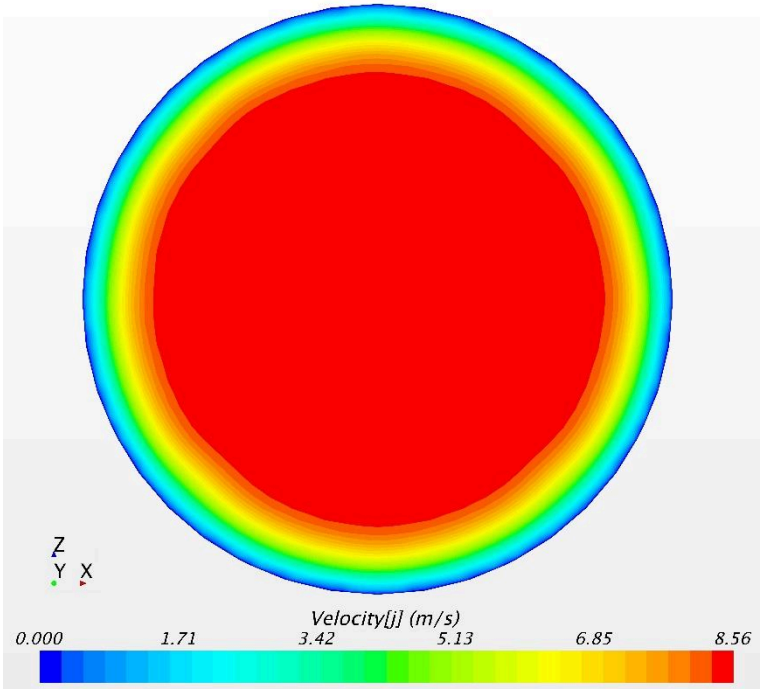

Figure 5 Contour map of the velocity distribution at the nozzle exit

3.4 Results and Discussions

It consumed about 2.8 ms to make the unsteady calculation reach a relatively stable state and then the calculation was continuously performed another 1 ms to obtain the time-averaged liquid jet trajectory. The contour map of volume fraction of acetone in the center plane of the calculation domain was shown in Figure 6. It can be seen from the figure that the liquid jet was uniformly cylindrical at the exit of the nozzle. With its development in the height direction, under the action of crossflow aerodynamics, the jet was gradually deflected downstream.

It can be seen from Figure 6 that the penetration height of the liquid jet was only about one-third of the height of the crossflow channel. Considering the vertical velocity distribution tested in the experiment, it can be inferred that the crossflow velocity corresponding to the root of the liquid column was lower than the average value of the crossflow velocity, and the crossflow velocity corresponding to the curved and breakup region at the top of the liquid column was greater than the average value of the crossflow velocity. The distribution of the crossflow velocity along the height direction will cause the change in crossflow and liquid column velocity discrepancy, and the discrepancy in crossflow and liquid column velocity was exactly the cause of K-H instability, which directly affected the breakup of the liquid column.

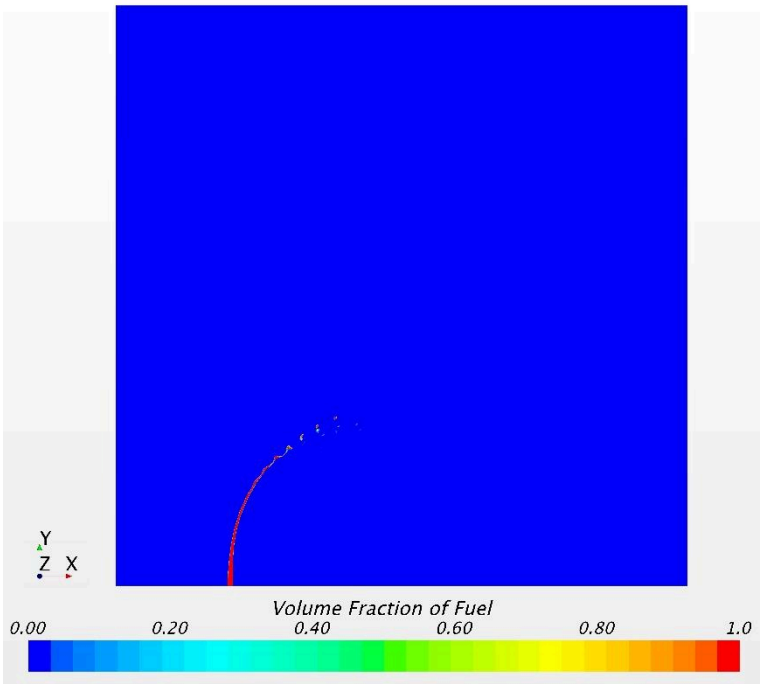

Figure 6 Contour map of volume fraction of acetone in the centre plane (t = 3.83 ms)

Figure 7 shows the boundaries of the liquid jet (the iso-surface with a volume fraction of liquid of 0.5) at different viewing angles. It can be seen from the figure that the round jet gradually became flat under the aerodynamic effect of crossflow, and the width of the liquid column on the windward side gradually increased in the Y direction. The K-H instability waves developed along the surface of the liquid column until the wavelength corresponded to the width of the liquid column. Due to the blockage of the liquid column, the crossflow decelerated and stagnated on the surface of the liquid column, causing the pressure on the windward surface of the liquid column to be greater than the pressure on the leeward side, as shown in Figure 8. Under the effect of the air pressure difference, a bag-shaped liquid membrane was formed. As the distance along the liquid column increased, the bag grew in the crossflow direction, and then gradually began to break up at the tip of the liquid column. The size of the droplets formed by the membrane was very small because the membrane was very thin at the point of breakup. Subsequently, the ring-shaped region with a larger diameter at the edge of the bag broke at the wave node. The two semi-circular liquid columns formed after the disconnection deformed into large-sized droplets under the action of surface tension then spread out to each side. The size of the droplets formed by the node itself was also large, and these big droplets flow downstream along the trajectory of the jet centre.

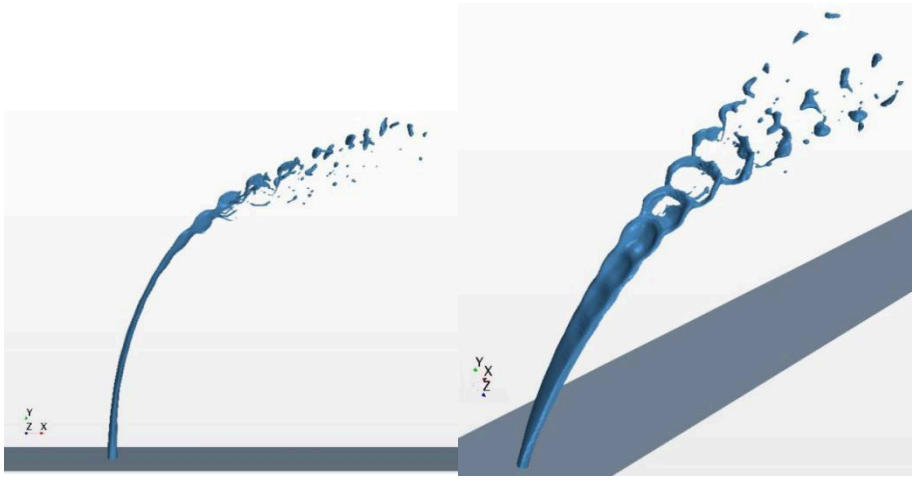

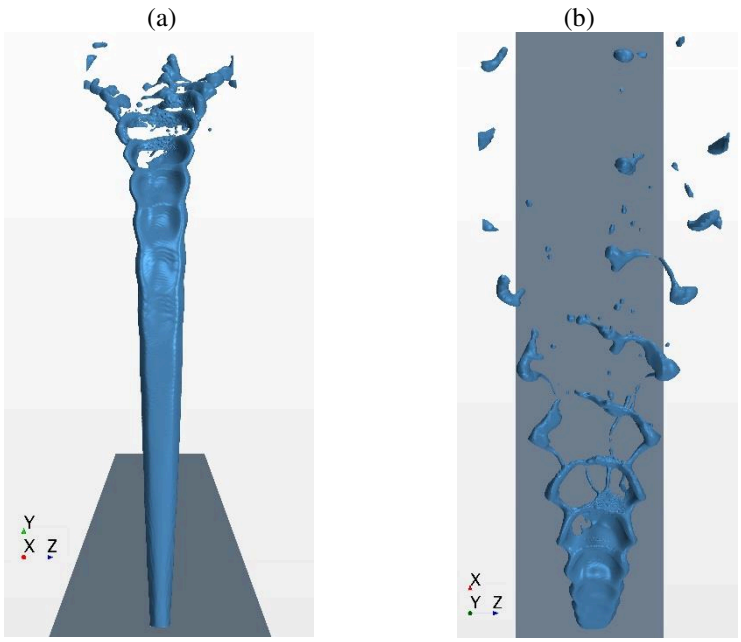

Figure 7 Various views of the boundaries of the liquid jet (t = 3.83 ms)

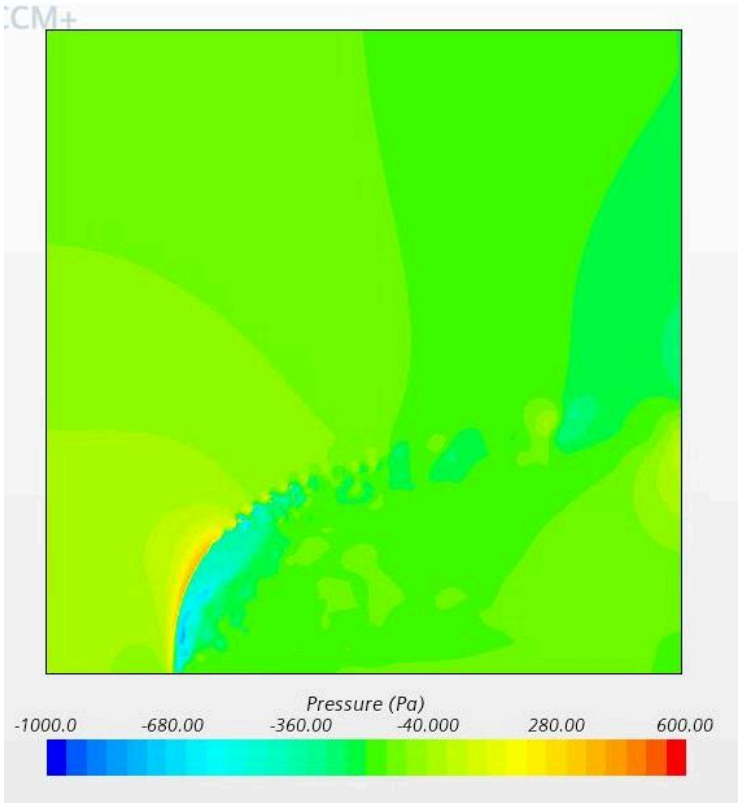

Figure 8 Contour map of gauge pressure in the centre plane (t = 3.83 ms)

The comparison of the simulation result of the liquid jet trajectory and penetration with experiment photo is illustrated in Figure 9. Although the simulation accurately described the main characteristics of the bag breakup, including the fluctuation of the surface of the liquid column, the initial formation and deformation of the bag, and the breakup of the wave node, compared with the experimental photo, the simulation still cannot capture the detail feature of the membrane near the deformation limit and breakup.

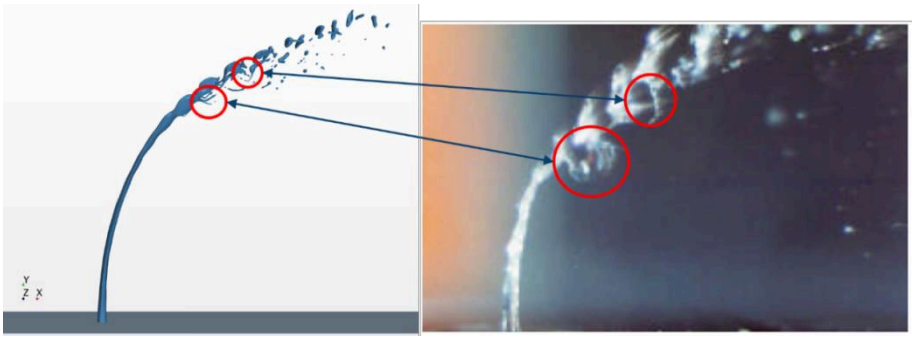

Figure 9 Comparison of the simulation result with experiment photo (t = 3.83 ms)

Wang et al.[19] investigated the bag breakup process of round liquid jets in crossflows. The formation and breakup process of bags in a water jet was shown in Figure 10. The figure showed that although in the early stage of bag development, the membrane on the tip of the bag was very thin. At this position, however, in the current study's numerical simulations, when the thickness of the membrane was less than the minimum mesh size, for the VOF model, the liquid phase was not continuous any more from a mathematical perspective. If the liquid phase is not continuous, the force balance between the pressure divergence and surface tension cannot be built up, hence the membrane cannot be formed. Furthermore, it was very difficult to accurately capture the precise phase boundary and find the right normal direction to establish the force balance of the membrane in a turbulent transient simulation. How to simulate all the details in bag breakup still needs further investigation.

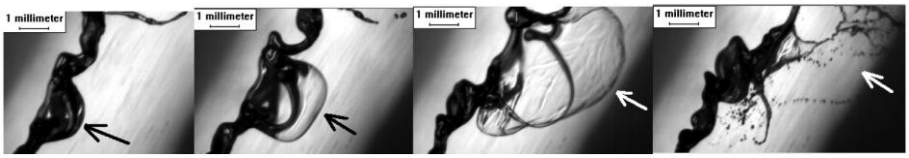

Figure 10 Bag breakup process of a water jet (Wang et al.[19])

An intuitive comparison of liquid jet trajectory is shown in Figure 11. It can be seen from the figure that when accurately simulating the velocity distribution of liquid jet and crossflow under the same experimental conditions, the numerical method used in this article can precisely simulate the trajectory and penetration of LJIC. In the range of $x/d_j < 20$, the error between the simulated LJIC trajectory and the experimental measurement was less than $\pm 5\%$.

The results show that the CFD is valid for predicting jet trajectory and main characteristics of the breakup but not for predicting the finer flow features associated with jet breakup.

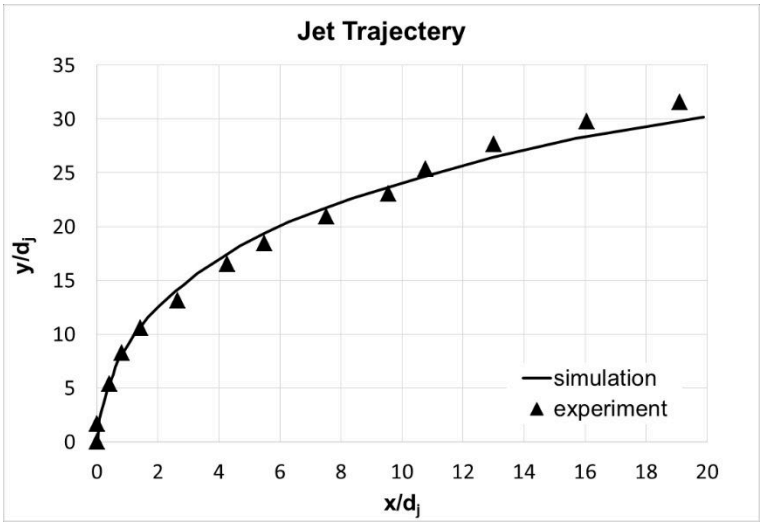

Figure 11 Comparison of the liquid jet trajectory (experiment data from Stenzler et al.[18])

4.0 SIMULATION OF LJIC AT REAL ENGINE CONDITION

After the validation in section 3, it can be considered that the existing numerical method can be used to simulate LJIC under real engine operating condition. Before the simulation, a real engine performance model was developed and the preliminary design of the combustor was completed to provide the proper physical model and flow boundary conditions for the LJIC simulation. The LEAP-1B engine was chosen to be the base model. A model of an engine similar to the LEAP-1B engine using information available in the public domain and making educated modelling assumptions (e.g. for component efficiencies, TET etc.) for information not available in the public domain was modeled using GasTurb (version 11) software. The general performance parameters of different working conditions and aero and thermal dynamic parameters at different stations were calculated. This article selected the cruise point at which engine had the longest working time and required higher atomization quality to achieve better temperature profile pattern at the outlet of the combustor for LJIC simulation. The sketch of the structure of the liner in the dome region was shown in Figure 12 (size in millimetre).

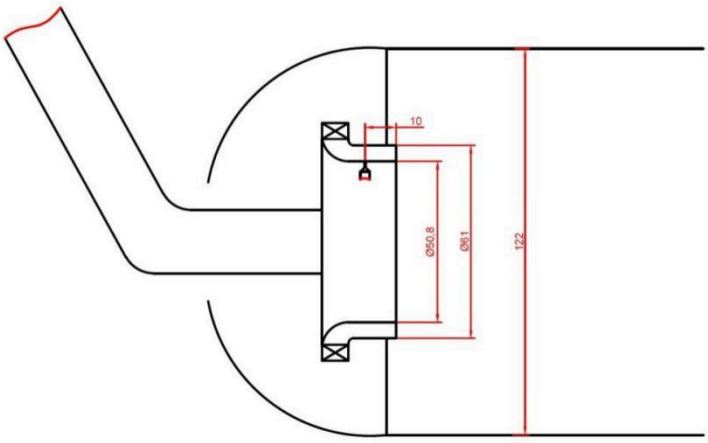

Figure 12 Sketch of the structure of the liner in dome region

4.1 Calculation Domain

Although the main stage passage was an annular channel in actual, in order to show the details of the flow conveniently, the sector calculation domain was transformed into a rectangular calculation domain. The size of the final calculation domain was 10×5.1×6

mm (Length × Height × Width) as shown in Figure 13. The axial position of the nozzle was 5 mm after the crossflow inlet.

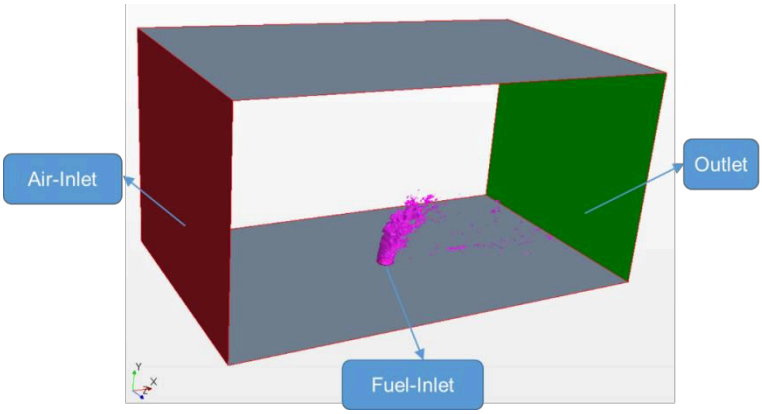

Figure 13 Schematic of the calculation domain

4.2 Calculation Grid

It is generally believed that when the droplet size is less than 0.01mm, the droplet tends to follow the airflow due to its small mass, which has little influence on the main breakup characteristics of the liquid jet. Considering that the main objects studied in this paper are liquid jet trajectory and primary breakup characteristics, the minimum grid size is set to 0.01mm here. The refined mesh is shown in Figure 14. After the final refinement, the size of the grid was 13.7 million approximately.

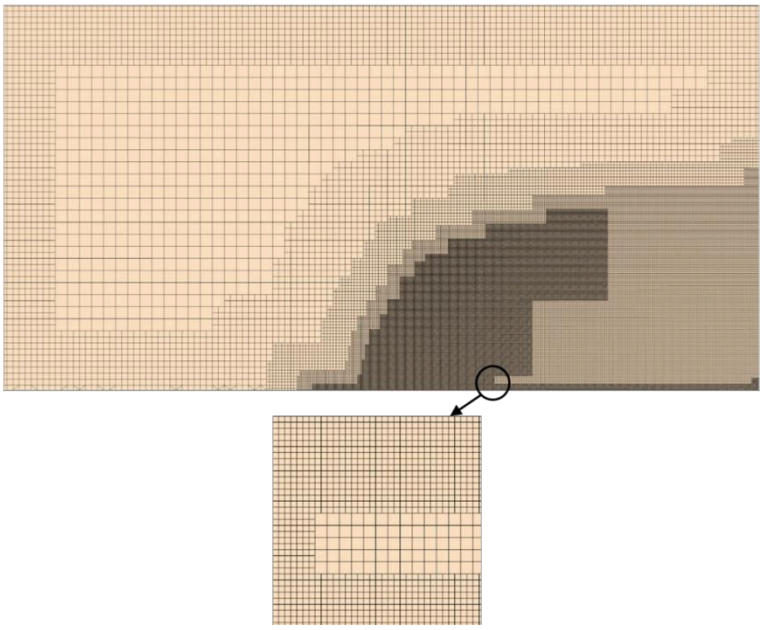

Figure 14 Mesh at center plane and zoomed view of mesh refinement

4.3 Boundary Conditions

The detailed boundary conditions for crossflow and liquid jet are shown in Table 3.

Table 3
Boundary conditions of crossflow and liquid jet

Jet diameter (d_j)	0.4 mm
Jet velocity (v_j)	16.53 m/s
Crossflow velocity (v_g)	121.9 m/s

Jet density (ρ_j)	721.4 kg/m^3
Crossflow density (ρ_g)	5.159 kg/m^3
Jet viscosity (μ_j)	3.51E-4 kg/m/s
Crossflow viscosity (μ_g)	3.33E-5 kg/m/s
Surface tension (σ)	0.01472 N/m
Crossflow pressure (P)	1.043 MPa
Jet temperature (T)	403 K
Crossflow temperature (T)	700 K
Momentum ratio (q)	2.57
Jet Weber number (We_j)	5356.3
Crossflow Weber number (We_g)	2083
Jet Reynolds number (Re_j)	13595.4
Crossflow Reynolds number (Re_g)	7548.7
Jet Ohnesorge number (Oh_j)	0.0054

The crossflow inlet velocity distribution used a fully developed turbulent velocity distribution, which was obtained from the simulation of a 200-times-passage-height-long channel, as shown in Figure 15. The geometry of the nozzle used a structure similar to that of the validation case, and the velocity distribution at the nozzle exit was shown in Figure 16.

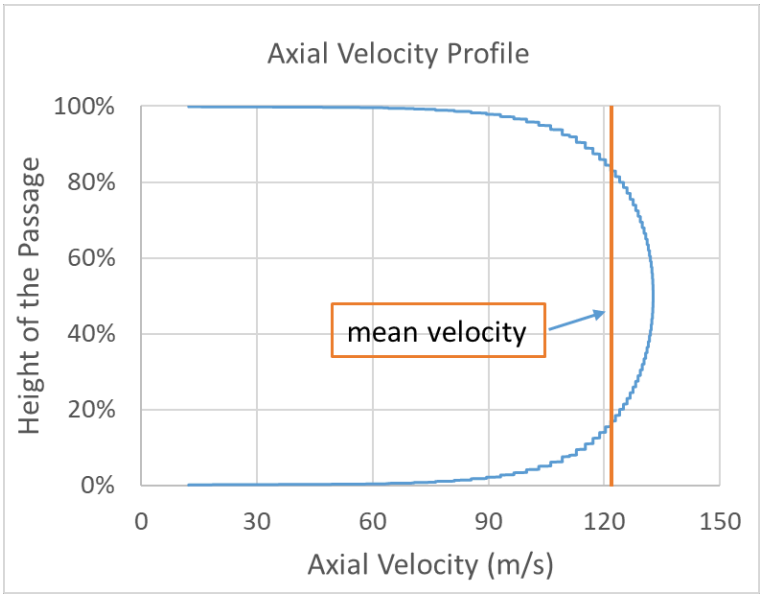

Figure 15 Velocity profile at the injection plane

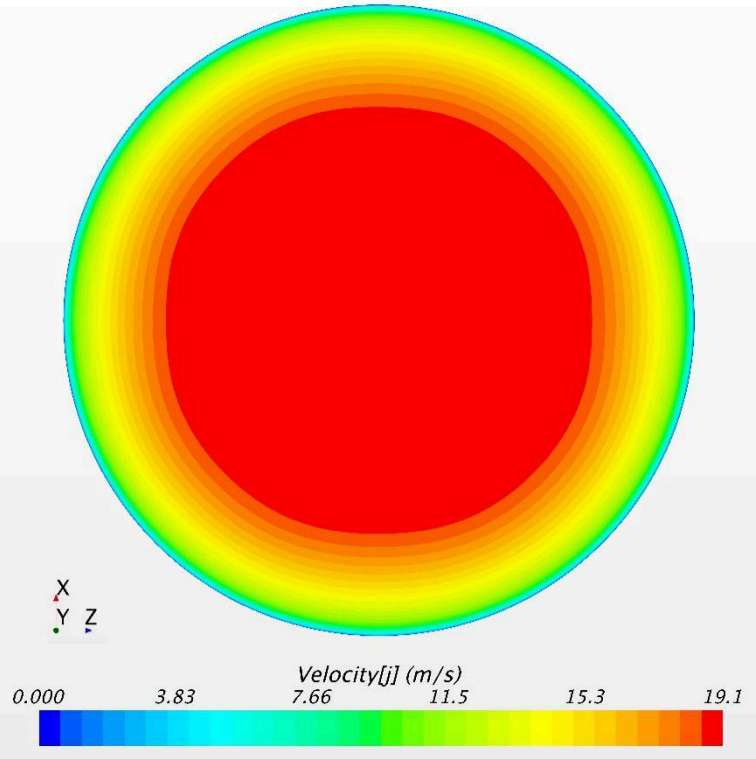

Figure 16 Contour map of the velocity distribution at the nozzle exit

4.4 Results and Discussions

The calculation was performed 0.19 ms.

4.4.1 Flow Field Structure

Figure 17 and Figure 18 showed the velocity distribution at the center plane and Y=1.25dj plane, respectively.

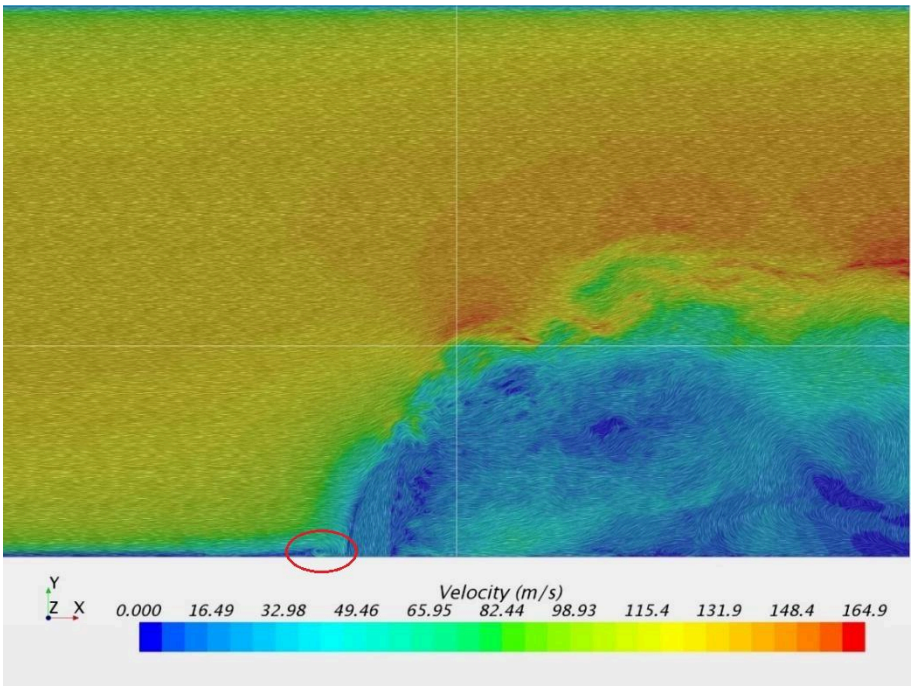

Figure 17 The velocity distribution at the center plane (t = 0.19 ms)

It can be seen from the figures that, due to the blocking effect of the liquid jet, the crossflow decelerated and stagnated on the windward side of the liquid jet, and the static pressure increased. The crossflow formed a small corner recirculation zone (the circle in Figure 17) at the front side of the liquid jet root. The stagnated crossflow accelerated along the windward side of the liquid jet, one part flowed up and one part flowed around the liquid column. A large area of low speed was formed downstream of the liquid column, which was full of irregular vortices of various sizes.

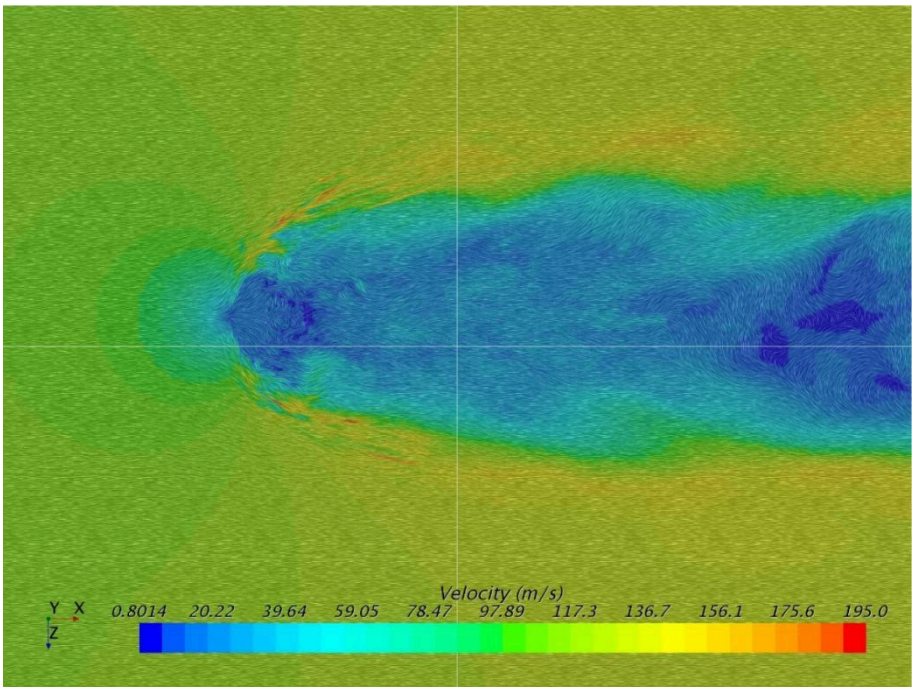

Figure 18 The velocity distribution at Y=1.25dj plane (t = 0.19 ms)

Figure 19 shows the temperature distribution at the center plane. Because the temperature of the liquid jet was low and the temperature of the crossflow was high, the interaction between the liquid jet and the crossflow was accompanied by heat exchange. But since the calculated time scale was very small, the degree of heat exchange was relatively low, and the temperature distribution also showed the distribution of the liquid spray in the flow field.

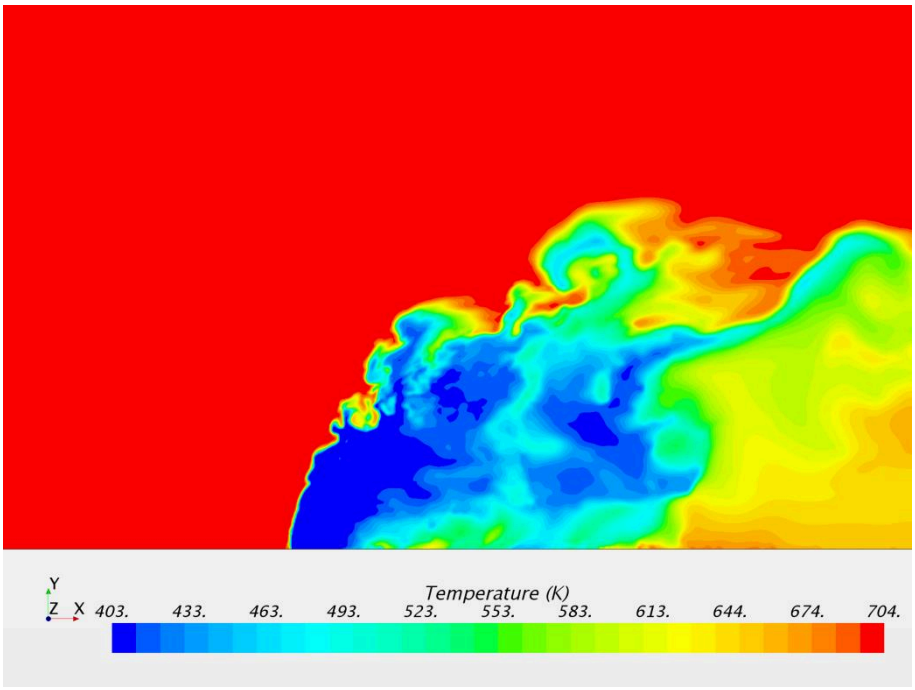

Figure 19 The temperature distribution at the center plane (t = 0.19 ms)

4.4.2 Breakup Mechanism

Figure 20 shows the boundaries of the liquid jet at different viewing angles. It can be seen that under real engine operating conditions, the breakup mode of LJIC was the surface shear breakup. The liquid column became flat under the aerodynamic force of the crossflow and bent downstream. The liquid column showed a small amount of deformation in the width direction. As the airflow accelerated on the surface of the liquid column, the velocity difference between the liquid column and the airflow on the gas-liquid boundary gradually increased, which causes the liquid surface to fluctuate due to K-H instability. The waves developed along the surface of the liquid column upwards and to both sides, forming a thin liquid film on the sides of the liquid column, and finally breaking into small droplets under the action of shear force. The size of the small droplets formed on the sides of the liquid column was very small (less than 0.01 mm in diameter), and the current grid size cannot show the subsequent movement of such small droplets in detail.

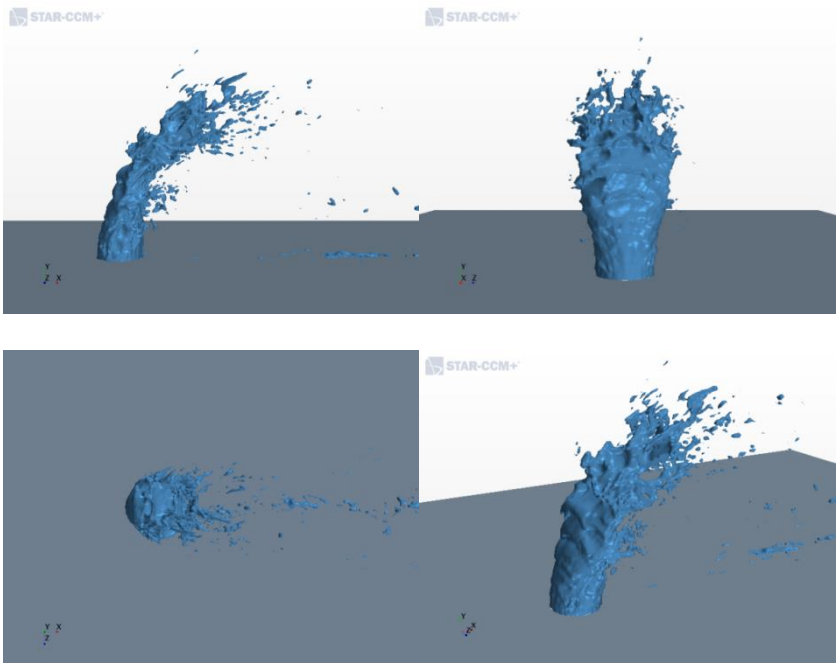

Figure 20 Various views of the boundaries of the liquid jet (t = 0.19 ms)

The contour map of the volume fraction of fuel in the center plane was illustrated in Figure 21. The time interval of each figure was 0.01 ms. It can be seen that this figure showed the full development period of a surface wave from the initial formation to the breakup at the tip of the liquid column. The initial wave was small, and the disturbance gradually increased as the airflow accelerated on the surface of the liquid. However, due to the surface tension of the liquid, the turbulent structure of the liquid surface eventually formed a vortex structure. The airflow decelerated and stagnated within the vortex, the static pressure increased, and a pressure difference was formed on the liquid vortex. The pressure differential drove the vortex to develop rapidly on the liquid surface, and finally broke into large droplets at the top of the liquid column, moved downstream along the edge of the liquid plume, and further broken up into small droplets under the action of aerodynamic force. The observation of the development of surface waves can provide references for subsequent experimental measurements, such as an appropriate high-speed camera response frequency is needed to capture the characteristics of surface waves.

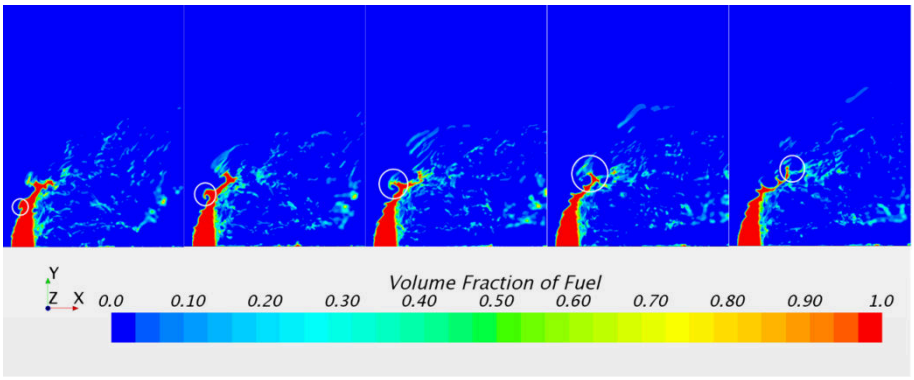

Figure 21 Contour map of volume fraction of fuel in the center plane

4.4.3 Trajectory of the LJIC

Figure 22 shows a comparison between the simulation result and the correlation predictions of the liquid jet trajectory.

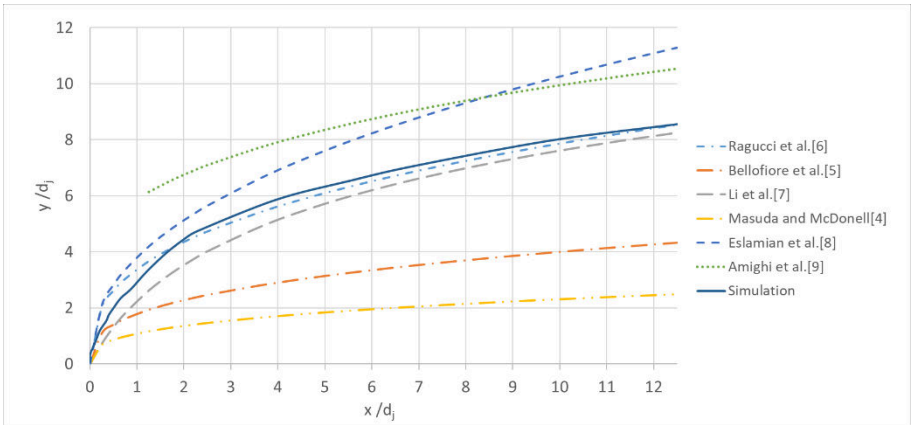

Figure 22 Comparison between the simulation result and the correlation prediction of the liquid jet trajectory

At the position $x/d_j = 12$ downstream of the nozzle, the penetration height of the liquid jet was about two-thirds of the height of the annular channel. Because the range of experimental conditions corresponding to different correlations and the boundary conditions of the velocity distribution of crossflow and liquid jets are very different, the results obtained by calculating the working conditions of this study with different correlations also show a big variation. This is not to say that the accuracy of these correlations is not good, but that it may not be suitable for the working conditions of this study. Compared with many correlations for predicting the trajectory of liquid jets, the simulation result was closest to the correlation of Ragucci et al.[6], and the accuracy of the simulation result has yet to be verified by subsequent experiments. Table 4 listed the comparison of the operating range provided by Ragucci and the simulation of this research. The trajectory of LJIC is affected by various parameters as listed in Table 4, as well as the velocity profile of both airflow and liquid jet. It can be seen from the comparison in Table 4 that the magnitude of q and T is closer, and there is a great difference of We_g and P. It can be preliminarily concluded that q and T have a greater impact on the trajectory of the liquid jet under typical aero-engine working conditions. But this is only a preliminary conclusion, which needs to be verified by experiments.

Table 4
Comparison of the operating range

	q	We_g	x/d_j	T(K)	P(bar)
Ragucci et al.	5–280	7-340	0–12	600	20
simulation	2.57	2083	0–12	700	10

5.0 CONCLUSIONS

In this research, an LJIC simulation using commercial CFD software was performed. When accurate flow boundary conditions are given, this simulation can accurately predict the jet trajectory of LJIC (with the prediction error less than ±5% at atmospheric conditions) and capture most of the flow details.

Through the simulation of LJIC under real engine operating conditions, the flow field characteristics were demonstrated, and the breakup mechanism of LJIC under high-temperature and high-pressure conditions was shown to be strong surface shear breakup mode. Under the research conditions of this project, the following correlation is most suitable for the prediction of LJIC trajectory. A database of numerical models was created to be further evaluated, validated and calibrated from a planned experimental campaign.

$$\frac{y}{d_j} = 2.28q^{0.422}\left(\frac{x}{d_j}\right)^{0.367} We_g^{-0.015}\left(\frac{\mu_g}{\mu_{air,300K}}\right)^{0.186}$$

The results can be used to guide the design of transverse jet atomizing nozzles in gas turbine combustor. At the preliminary design phase, the atomization and mixing distribution features with considerable accuracy can be obtained to shorten the research and development period and reduce the test cost.

ACKNOWLEDGMENTS

The authors gratefully acknowledge the financial support from the China Scholarship Council for Mr Yu Zhu which enabled him to enrol on, and complete the MSc Thermal Power Course at Cranfield University, where this research was conducted.

REFERENCES

[1] STICKLES, R., BARRETT, J., "TAPS II technology final report – Technology assessment open report," accessed April 11, 2020, from http://www.faa.gov/about/office_org/headquarters_offices/apl/research/aircraft_technology/cleen/reports/media/TAPS_II_Public_Final_Report.pdf, 2014.

[2] WU, P.-K., MIRANDA, R. F. AND FAETH, G. M. (1995) 'Effects of Initial Flow Conditions on Primary Breakup of Nonturbulent and Turbulent Round Liquid Jets', *Atomization and Sprays*, 5(2), pp. 175–196. doi: 10.1615/AtomizSpr.v5.i2.40.

[3] WU, P.-K., KIRKENDALL, K. A., FULLER, R. P. AND NEJAD, A. S. (1997) 'Breakup Processes of Liquid Jets in Subsonic Crossflows', *Journal of Propulsion and Power*, 13(1), pp. 64–73. doi: 10.2514/2.5151.

[4] MASUDA, B. J., MCDONELL, V. G., "Penetration of a recessed distillate liquid jet into a crossflow at elevated pressure and temperature," *ICLASS 2006 10th International Conference on Liquid Atomization and Spray Systems*, Kyoto, Japan, 2006.

[5] BELLOFIORE, A., CAVALIERE, A. RAGUCCI, R., "Air density effect on the atomization of liquid jets in crossflow," *Combustion Science and Technology*, vol. 179, no. 1-2, pp. 319-342, 2007.

[6] RAGUCCI, R., BELLOFIORE, A., CAVALIERE, A., "Breakup and breakdown of bent kerosene jets in gas turbine conditions," *Proceedings of the Combustion Institute*, 31 II, pp. 2231–2238, 2007.

[7] LI, L., LIN, Y., XUE, X., GAO, W., SUNG, C. J., "Injection of liquid kerosene into a high-pressure subsonic air crossflow from normal temperature to elevated temperature," *Proceedings of the ASME Turbo Expo*, pp. 877-884, 2012.

[8] ESLAMIAN, M., AMIGHI, A., ASHGRIZ, N., "Atomization of liquid jet in high-pressure and high-temperature subsonic crossflow," *AIAA Journal*, vol. 52, no. 2, pp. 1374-1385, 2014.

[9] AMIGHI, A. and ASHGRIZ, N., "Trajectory of a liquid jet in a high temperature and pressure gaseous cross flow," *Journal of Engineering for Gas Turbines and Power*, vol. 141, no. 6, pp. 061019, 2019.

[10] NG, C. L., SALLAM, K. A., METWALLY, H. M., AALBURG, C., "Deformation and surface waves properties of round nonturbulent liquid jets in gaseous crossflow," *Proceedings of 2005 ASME Fluids Engineering Division Summer Meeting, FEDSM2005*, pp. 2432–2436, 2005.

[11] LI, X., SOTERIOU, M. C., HARTFORD, E., "High-fidelity simulation of high density-ratio liquid jet atomization in crossflow with experimental validation," *ILASS Americas 26th Annual Conference on Liquid Atomization and Spray Systems*, Portland, OR, 2014.

[12] LI, X., SOTERIOU, M. C., "High fidelity simulation and analysis of liquid jet atomization in a gaseous crossflow at intermediate weber numbers," *Physics of Fluids*, vol. 28, no. 8, 2016.

[13] LI, X., SOTERIOU, M. C., "Detailed numerical simulation of liquid jet atomization in crossflow of increasing density," *International Journal of Multiphase Flow*, Elsevier Ltd, 104, pp. 214–232, 2018.

[14] XIAO, F., DIANAT, M., MCGUIRK, J. J., "Large eddy simulation of liquid-jet primary breakup in air crossflow," *AIAA Journal*, vol. 51, no. 12, pp. 2878-2893, 2013.

[15] FARVARDIN, E., DOLATABADI, A., "Simulation of biodiesel jet in cross flow," *ICLASS 2012 12th Triennial International Conference on Liquid Atomization and Spray Systems*, Heidelberg, Germany, 2012.

[16] PAI, M., PITSCH, H., DESJARDINS, O., "Detailed numerical simulations of primary atomization of liquid jets in crossflow," *47th AIAA Aerospace Sciences Meeting including The New Horizons Forum and Aerospace Exposition*, Reston, Virigina, 2009.

[17] HERRMANN, M., ARIENTI, M., SOTERIOU, M., "The impact of density ratio on the liquid core dynamics of a turbulent liquid jet injected into a crossflow," *Journal of Engineering for Gas Turbines and Power*, vol. 133, no. 6, pp. 061501, 2011.

[18] STENZLER, J., LEE, J., SANTAVICCA, D., "Penetration of liquid jets in a crossflow," *41st AIAA Aerospace Sciences Meeting and Exhibit*, Reston, Virigina, 2003.

[19] WANG, X.-H, HUANG, Y., WANG, S.-L., LIU, Z.-L., "Bag breakup of turbulent liquid jets in crossflows," *AIAA Journal*, vol. 50, no. 6, pp. 1360-1366, 2012.

2021-09-13

Numerical investigation of the breakup mode and trajectory of liquid jet in a gaseous crossflow at elevated conditions

Zhu, Yu

Cambridge University Press

Zhu Y, Sun X, Sethi V, et al., (2021) Numerical investigation of the breakup mode and trajectory of liquid jet in a gaseous crossflow at elevated conditions. The Aeronautical Journal, Volume 125, Issue 1291, September 2021, pp. 1519-1541

https://doi.org/10.1017/aer.2021.10